ACSNANO
www.acsnano.org
ARTICLE

ZnO-Based Nanoplatforms for Labeling and Treatment of Mouse Tumors without Detectable Toxic Side Effects

Dai-Xin Ye,[†] Ying-Ying Ma,[†] Wei Zhao,[†] Hong-Mei Cao,[†] Ji-Lie Kong,[*,†,‡] Huan-Ming Xiong,[*,†] and Helmuth Möhwald[§]

[†]Department of Chemistry, Fudan University, Shanghai 200433, P. R. China
[‡]Institutes of Biomedical Sciences, Fudan University, Shanghai 200032, P. R. China
[§]Max-Planck Institute of Colloids and Interfaces, Potsdam 14424, Germany

Supporting Information

ABSTRACT: **ZnO quantum dots (QDs) were synthesized with polymer shells, coordinated with Gd^{3+} ions and adsorbed doxorubicin (DOX) together to form a new kind of multifunctional ZnO-Gd-DOX nanoplatform. Such pH sensitive nanoplatforms were shown to release DOX to cancer cells *in vitro* and to mouse tumors *in vivo*, and reveal better specificity and lower toxicity than free DOX, and even better therapeutic efficacy than an FDA approved commercial DOX-loading drug DOX-Liposome Injection (DOXIL, NDA#050718). The ZnO-Gd-DOX nanoplatforms exhibited strong red fluorescence, which benefited the fluorescent imaging on live mice. Due to the special structure of ZnO-Gd-DOX nanoparticles, such nanoplatforms possessed a high longitudinal relaxivity r_1 of 52.5 mM^{-1} s^{-1} at 0.55 T, which was superior to many other Gd^{3+} based nanoparticles. Thus, both fluorescence labeling and magnetic resonance imaging could be applied simultaneously on the tumor bearing mice along with drug delivery. After 36 days of treatment on these mice, ZnO-Gd-DOX nanoparticles greatly inhibited the tumor growth without causing any appreciable abnormality in major organs. The most important merit of ZnO-Gd-DOX was that such a nanoplatform was biodegraded completely and showed no toxic side effects after H&E (hematoxylin and eosin) staining of tumor slices and ICP-AES (inductively coupled plasma atomic emission spectrometry) bioanalyses.**

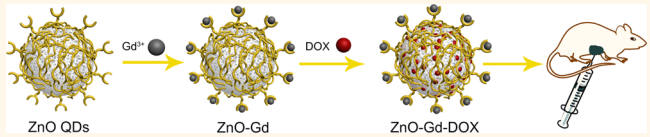

KEYWORDS: *ZnO, anticancer, drug delivery, fluorescent imaging, magnetic resonance imaging*

Cancer is threatening human health dreadfully over the world.[1,2] The current cancer treatments mainly employ radiotherapy and chemotherapy, which destroy the normal cells and healthy tissues during treatments and eventually the immunity of the patients.[3,4] New therapeutic techniques with high specificity are urgently required to release anticancer agents intelligently to the cancerous cells inside the complex microenvironment of tumors.[5] Meanwhile, the treatment processes and the therapy effects have become amenable to be monitored simultaneously by labeling techniques, such as magnetic resonance imaging (MRI) and fluorescence imaging.[6−8] Among the various intelligent nanoplatforms carrying medicines and labeling agents,[9−12] nanoparticles (NPs) have become the most popular candidates because their sizes, shapes, and surface groups can be precisely controlled by chemical syntheses. Thus, the drawbacks of the conventional anticancer drugs concerning water solubility,[13,14] targeting capability[15,16] and systemic toxicity[17,18] have been overcome. These NPs include metal oxide NPs,[19,20] rare earth NPs,[21,22] carbon NPs,[23,24] carbon nanotubes,[25,26] graphene,[27,28] mesoporous silica NPs,[29−31] polymer NPs,[32,33] *etc.* Although the drug delivery systems (DDSs) based on these NPs have shown promising therapeutic efficacy, most of them are not biodegradable and many of them cannot be excreted by animals, which form unexpected potential toxicity chronically.[34−36] Furthermore, for a multifunctional nanoplatform, its different functions always interfere with each other. For example, magnetic ions often quench the fluorescence of quantum dots, and a complex core−shell structure enhances the stability but renders a low entrapment efficiency and an even lower release rate of drugs. In fact, it is still a challenge to prepare multifunctional DDSs with simultaneously high ratios of drug loading and release, rapid and specific responses toward the tumor environment, high resolution of imaging *in vivo*, no toxic residues, and satisfying cure rates.

ZnO quantum dots (QDs), as a kind of versatile and low cost material, have gained practical applications in biomedical

Received: December 13, 2015
Accepted: March 24, 2016
Published: March 28, 2016

DOI: 10.1021/acsnano.5b07846
ACS Nano 2016, 10, 4294−4300

areas.[37−41] Since ZnO is listed as a safe substance by the United States Food and Drug Administration (21CFR182.8991) and it is stable toward air and sunlight, ZnO nanoparticles are often added into commercial sunscreen cream for absorbing UV light. ZnO-based antimicrobial agents are also applied for skin protection commercially, especially in baby diapers and children dermatitis treatment. In previous reports, fluorescent probes based on ZnO QDs exhibited tunable photoluminescence (PL), high photostability and low toxicity both *in vitro*[38,42] and *in vivo*.[43−45] With respect to drug delivery, our research group employed ZnO QDs to carry anticancer drugs, and the obtained DDS showed high drug loading and release ratios, instant pH response and complete biodegradation in the lysosomes of brain cells.[16] In the latest achievements by Kim *et al.*[46] and Zhang *et al.*,[47] ZnO-based core−shell NPs were successfully applied to deliver drugs to mice *in vivo*, but the biodegradation or excretion of those large NPs remained troublesome. Moreover, the Fe_3O_4 component rendered ZnO fluorescence very weak,[46] and the Gd^{3+} ions encapsulated in the complex core−shell nanoparticles[47] exhibited a longitudinal relaxivity r_1 of only 4.78 mM^{-1} s^{-1}.

Herein, we introduce an intelligent biodegradable DDS composed of ZnO QDs, Gd^{3+} ions, and doxorubicin (DOX). This ZnO-Gd-DOX nanoplatform possesses excellent water solubility, biocompatibility, and pH sensitivity and can release DOX sustainably into the acid environment of tumors. It is also a bifunctional probe for both fluorescent imaging and MRI. On one hand, the strong red emission of ZnO-Gd-DOX in the range of 600−800 nm makes it suitable for animal imaging, thus overcoming the limitation of ZnO visible emission which needs UV irradiation and only varies from blue to yellow. On the other hand, Gd^{3+} ions are fixed stably on the ZnO surface through proper coordination with the carboxyl groups. Such a structure ensures plenty of water molecules surrounding Gd^{3+} ions and renders a longitudinal relaxivity r_1 of 52.5 mM^{-1} s^{-1}, which is much higher than that of the clinical Gd-DTPA agent. Human pancreatic cancer (BxPC-3) tumor-bearing mice were injected with such ZnO-Gd-DOX solution, and monitored by both fluorescent imaging and MRI clearly. After circulation, the ZnO-Gd-DOX NPs were totally biodegraded and most of Zn^{2+} and Gd^{3+} ions were excreted from the mice body. In comparison with both free DOX and an FDA approved commercial DOX-loading drug DOX-Liposome Injection (DOXIL, NDA#050718), our ZnO-Gd-DOX NPs exhibited both better chemotherapy efficacy and lower toxicity, as will be demonstrated in detail below.

RESULTS AND DISCUSSION

Synthesis and Characterization of ZnO-Gd-DOX NPs. Highly luminescent water-soluble ZnO@polymer core−shell QDs were prepared by a two-step copolymerization method,[42] in which the synthetic conditions were adjusted critically to obtain excess carboxyl groups on ZnO surfaces. Afterward, Gd^{3+} ions were introduced onto ZnO surfaces through coordination with the carboxyl groups. Since the as-prepared ZnO QDs surfaces are negatively charged on their surfaces, they can adsorb positive DOX by both the strong electrostatic interactions and the coordination effects,[48] as proved by zeta potential measurements (Figure S1). Both the dynamic light scattering (DLS) data (Figure S2) and transmission electron microscopy (TEM) images (Figure 1) confirm that the final ZnO-Gd-DOX NPs are uniform and monodispersed stably in water. The ZnO particle size in TEM images looks smaller than

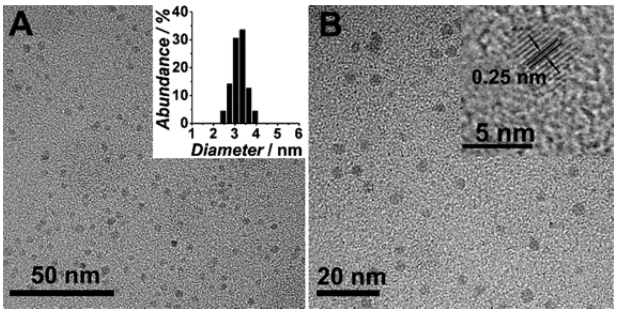

Figure 1. (A) TEM image and (inset) size distribution of ZnO-Gd NPs. (B) TEM image and (inset) HRTEM of ZnO-Gd-DOX NPs.

that in DLS data because the DLS results include the polymer shells, DOX, and the surrounding water molecules. The averaged distance between the ZnO lattices is about 0.25 nm, corresponding to the (101) planar spacing of the wurzite structure,[39] in accord with the X-ray diffraction patterns (Figure S3), indicating that Gd^{3+} incorporation has no influence on the ZnO lattice.[49] In addition, the ICP-AES (inductively coupled plasma atomic emission spectroscopy) measurement reveals the Gd/Zn molar ratio of 0.17 in the whole ZnO-Gd NPs, and the energy dispersive spectroscopy (EDS) of the ZnO-Gd NPs confirms the location of Gd^{3+} ions (Figure S4) on ZnO surfaces. The weight percentages of polymer, ZnO, Gd, and DOX in ZnO-Gd-DOX were measured to be 65.0%, 13.4%, 4.4%, and 17.2%, respectively.

Optical and Magnetic Resonance Contrast Properties of ZnO-Gd-DOX NPs. In Figure 2A, ZnO-Gd NPs exhibit the UV absorption due to the ZnO band gap transition and the typical green fluorescence related with ZnO defects.[39] These optical features change dramatically after DOX loading. The

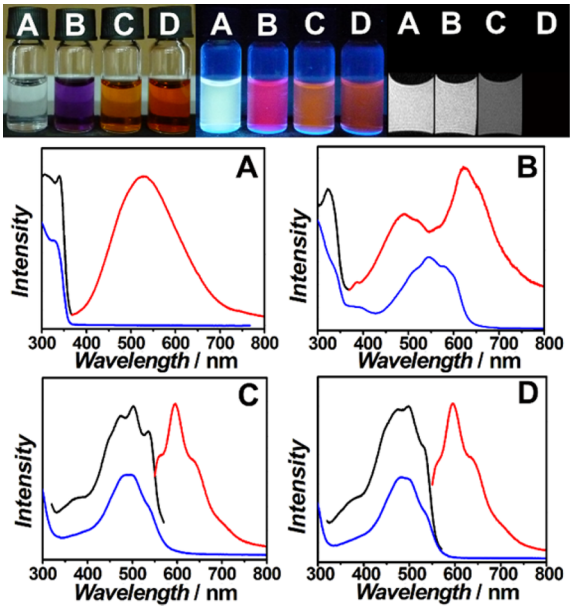

Figure 2. Top: photos of (A) ZnO-Gd, (B) ZnO-Gd-DOX, (C) ZnO-Gd-DOX decomposed at pH 5.0, and (D) free DOX, in daylight (left), under UV light (middle), and their T_1-weighted MR images (right), respectively. Bottom: UV−vis absorption (blue), PL excitation (black), and PL emission (red) spectra of these samples. Both samples A and B are excited at 340 nm with a 399 nm optical filter, while samples C and D are excited at 500 nm.

DOI: 10.1021/acsnano.5b07846
ACS Nano 2016, 10, 4294−4300

ZnO-Gd-DOX has purple color in daylight because the coordination between ZnO and DOX causes a red shift of the DOX absorption. However, the red emission under UV light is amazing and quite different from that of ZnO@polymer-DOX in our previous work,[16] because it is never a simple overlap of ZnO emission and DOX emission. In ZnO-Gd-DOX, the main emission peak of DOX redshifts from 595 to 625 nm and the whole PL emission intensity within 600–800 nm is greatly enhanced. The red fluorescence is suggested to arise from DOX, but without ZnO, the sample only shows typical free DOX spectra like Figure 2D. Such unique PL features of ZnO-Gd-DOX may be attributed to the fluorescence resonance energy transfer (FRET) from ZnO to DOX, and the complex interactions between ZnO, Gd^{3+}, and DOX. After decomposition at pH 5.0, the sample in Figure 2C exhibits the same optical features as free DOX in Figure 2D, indicating that DOX molecules are released without any change. Figure S5 illustrates that more than 90% of the DOX molecules are released within 10 h under this condition, just like in the acid environment of tumors. Under a 0.55 T MRI system, the longitudinal relaxivity r_1 and the transverse relaxivity r_2 of ZnO-Gd were determined to be 49.5 and 63.0 mM^{-1} s^{-1}, respectively,[50] while those of ZnO-Gd-DOX were even larger (52.5 and 66.5 mM^{-1} s^{-1} for r_1 and r_2). For comparison, the commercial Gd-DTPA shows much smaller relaxivities (3.7 and 4.2 mM^{-1} s^{-1} for r_1 and r_2) at the same conditions (Figure 3A). Figure 3B shows that r_1 of ZnO-Gd and ZnO-Gd-DOX remained stable within 15 days, so there were neither leached Gd^{3+} ions[51] nor NPs aggregation.[34]

Figure 3C compares the T_1-weighted MRI of the samples with the same Gd^{3+} concentrations. ZnO-Gd and ZnO-Gd-DOX induce a much more significant T_1 signal enhancement than Gd-DTPA and $GdCl_3$. Among those reported Gd^{3+} based agents in Tables S1 and S2, our products possess outstanding relaxivities due to their structural merits. First, in comparison

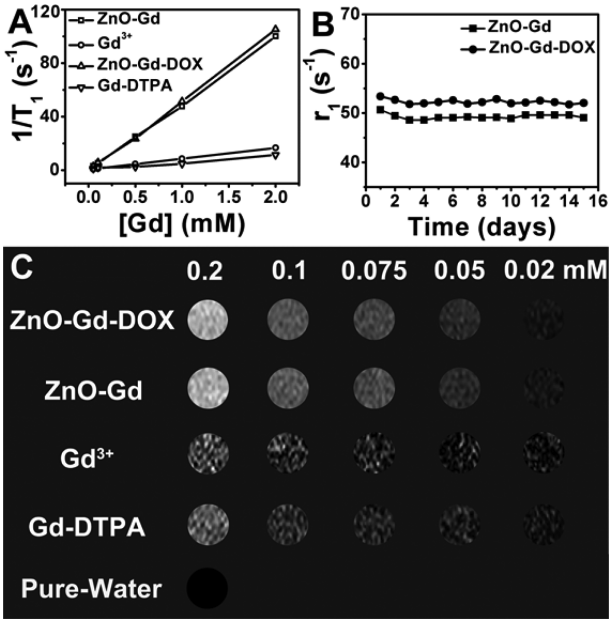

Figure 3. (A) The longitudinal relaxation curves of ZnO-Gd-DOX, ZnO-Gd, Gd-DTPA, and $GdCl_3$ at 0.55 T. (B) Evolution of r_1 values of ZnO-Gd-DOX and ZnO-Gd aqueous solutions in 15 days. (C) T_1-weighted MRI at various Gd^{3+} concentrations of the above samples and pure water at 0.55 T.

with the Gd^{3+}–ligand complexes, the attachment of Gd^{3+} ions onto ZnO NPs increases the hydrodynamic radius and thus improves r values due to the Debye-Stokes equation.[51] Second, the relaxivity of Gd^{3+} ions is basically proportional to the relaxation of the neighboring water molecules which are coordinated directly with the Gd^{3+} ions.[52] Since Gd^{3+} ions are attached on ZnO surfaces, a large amount of water molecules are surrounding Gd^{3+} ions in aqueous solutions, and thus, ZnO-Gd NPs exhibit much higher relaxivities than those core–shell NPs in which Gd^{3+} ions are confined in the solid cores.[47] Third, the payload of Gd^{3+} ions on each particle determines the total relaxivity of the contrast agent. Although our ZnO QDs are only 3 nm in diameter, there are on average 148 Gd^{3+} ions coating on each ZnO particle, and such a payload per unit area is much larger than those of many other NP–Gd^{3+} composites.[53]

Confocal Fluorescence Imaging and Magnetic Resonance Imaging. ZnO-Gd-DOX NPs were injected to the tumors of mice and emitted strong red fluorescence (Figure 4A–C), which is superior over many other ZnO-based

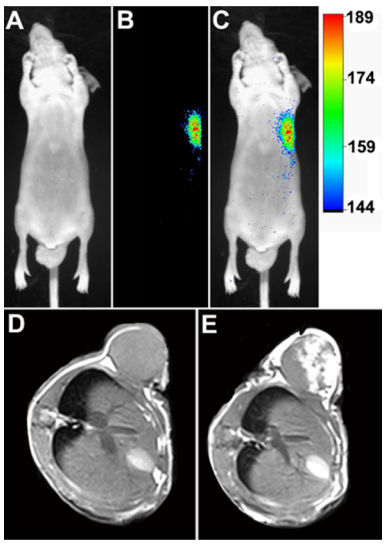

Figure 4. *In vivo* fluorescent images of BxPC-3 tumor-bearing nude mice under (A) bright field and (B) laser irradiation after intratumor injection of ZnO-Gd-DOX (100 μL, 2 mg/mL). (C) Overlay of (A) and (B). The T_1-weighted images of the same mice (D) before injection and (E) 2 h after intratumor injection of ZnO-Gd-DOX.

fluorescence probes because the typical fluorescence of ZnO nanoparticles can only be tuned from blue to yellow.[37] For three-dimensional location of the tumor with an anatomical resolution, the mice were tested by the T_1-weighted MRI technique, and the section in Figure 4E was significantly brightened by the contrast agent, with its intensity about 4 times higher than that of the tumor injected by physiological saline (Figure 4D). The combination of such two types of imaging abilities endows ZnO-Gd-DOX with potential application in the imaging guided therapy.

Therapy and Toxicity to Mice. BxPC-3 tumor-bearing nude mice were injected with different agents to study chemotherapy efficacy. Figure 5A showed that the tumors receiving physiological saline grew rapidly and the commercial DOXIL could suppress tumor growth, but both DOX and ZnO-Gd-DOX performed much better than DOXIL. Figure 5B

DOI: 10.1021/acsnano.5b07846
ACS Nano 2016, 10, 4294–4300

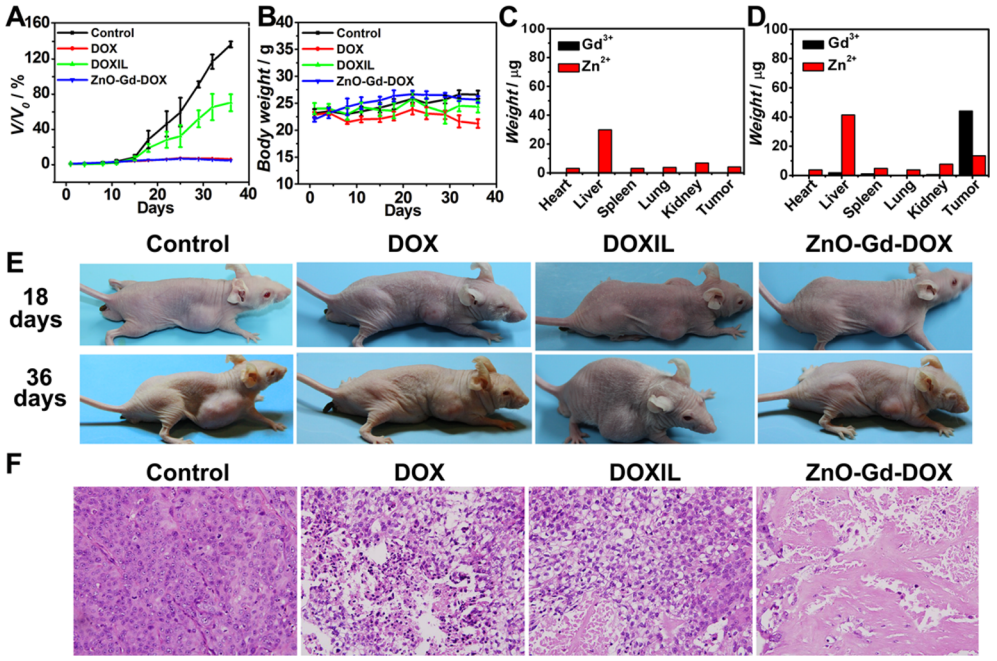

Figure 5. (A) The tumor volume growth *V versus* the initial volume V_0 under different treatments. (B) Body weight changes of mice during parallel treatments, in which the dosages of free DOX and ZnO-Gd-DOX are the same 2 mg/kg of DOX in each injection. Quantitative analyses of Zn and Gd content in major organs collected from the mice treated with (C) saline and (D) ZnO-Gd-DOX NPs after 36 days. (E) Images of BxPC-3 tumor-bearing nude mice after 18 and 36 days under different treatments. (F) H&E staining of tumor slices after 36 days of treatments by different agents.

compares the body weight evolution of these mice. Although both the control and the ZnO-Gd-DOX treated mice kept growing simultaneously, the weight improvement of the control was mainly caused by the tumor growth (Figure 5E). In contrast, the weight decrease of the free DOX treated mice indicated strong toxic side effects of the free DOX. H&E (hematoxylin and eosin) staining of tumor slices (Figure 5F) showed that the cells in the control retained their normal membrane and nuclear structures, and the cells treated by DOX or DOXIL were damaged partly, while almost all cells were severely destroyed after ZnO-Gd-DOX treatment. In general, the chemotherapy results in Figure 5 confirmed that ZnO-Gd-DOX NPs performed better than the other agents.

Besides the tumors, all of the major organs of mice were also studied by the histological examinations by H&E staining, and the results revealed no damage or inflammatory lesion (Figure S8). Furthermore, the distributions of Zn^{2+} and Gd^{3+} ions in heart, liver, spleen, lung, kidney, and tumor were analyzed by ICP-AES measurement. The results showed no Gd^{3+} ions were detected in the saline treated mice, but their all organs could enrich Zn^{2+} ions, especially the liver (Figure 5C). In contrast, there were more Zn^{2+} ions in the liver of the mice injected with ZnO-Gd-DOX NPs, while Gd^{3+} ions mainly located in the tumor (Figure 5D). The contrast between Figure 5C and 5D clearly shows most of the Zn^{2+} and Gd^{3+} ions from ZnO-Gd-DOX were excreted by mice after 36 days. Therefore, the toxic side effects from Zn^{2+} and Gd^{3+} ions were negligible. In addition, the HPLC analyses of leftover DOX showed that the average DOX concentration in the livers receiving DOXIL was 42.43 ng/g, much higher than that of the livers receiving ZnO-Gd-DOX (16.06 ng/g). All results proved that ZnO-Gd-DOX NPs had almost no toxic side effects to mice, and they were biodegraded and excreted finally.

To determine whether the therapy effects of ZnO-Gd-DOX NPs result from the ZnO or Gd component, the cytotoxicities of DOX, ZnO-Gd, and ZnO-Gd-DOX were evaluated by the conventional MTT assays after incubation with BxPC-3 cells for 24 h, respectively. The results confirmed that ZnO-Gd NPs were nontoxic even when the Zn^{2+} ions concentration was as high as 8 μg/mL, while both ZnO-Gd-DOX NPs and DOX were vital to BxPC-3 cells when the corresponding DOX concentrations were only 4 μg/mL (Figure S9). ZnO-Gd NPs were also injected into the tumors of BxPC-3 tumor-bearing nude mice every 2 days and monitored closely for 36 days. Figure S10 shows that the tumors receiving ZnO-Gd grew rapidly, which was nearly the same as for the tumors receiving physiological saline, and thus, the tumor growth was affected by neither ZnO QDs nor Gd^{3+} ions. Moreover, both the ZnO-Gd treated mice and the control group showed a similar body weight evolution, indicating that the repeated intratumor injections did no harm to mice. The ZnO-Gd treated mice were also sacrificed to study the H&E staining slices of the tumor and the major organs (Figure S11). Only few of the tumor cells were damaged by ZnO-Gd NPs and no damage or inflammatory lesion was observed in all major organs. Therefore, the therapy effects of ZnO-Gd-DOX NPs both *in vitro* and *in vivo* were mainly from DOX, but much better than those from free DOX alone.

CONCLUSIONS

In summary, a multifunctional ZnO-Gd-DOX nanoplatform for diagnosis and treatment on mice tumors *in vivo* has been developed with at least five advantages. First, ZnO QDs as the cores of such a nanoplatform can be biodegraded completely in the acidic environment of tumors and their excellent pH responsiveness ensures the specificity of drug delivery to cancer cells. Second, the polymer shells kept ZnO QDs dispersed

DOI: 10.1021/acsnano.5b07846
ACS Nano 2016, 10, 4294–4300

stably in aqueous solutions on one hand, and on the other, their excess carboxyl groups coordinated with many Gd^{3+} ions, which rendered an outstanding relaxivity for MRI. Third, the combination of highly luminescent ZnO QDs and DOX produces strong fluorescence in the range of 600−800 nm, which benefits the fluorescence imaging *in vivo*. Fourth, ZnO-Gd-DOX NPs showed better therapeutic efficacy than DOX and DOXIL, which can be ascribed to the specificity of such a nanoplatform toward tumors. Finally, ZnO-Gd-DOX NPs had no detectable toxic side effects to mice, and the whole NPs could be biodegraded and excreted from the mice body. All these merits are based on the carefully selected composition and the well-designed structure of such unique nanoplatform, which promises a bright future of ZnO NPs based platforms for chemotherapy.

MATERIALS AND METHODS

Syntheses and Characterizations of ZnO-Gd and ZnO-Gd-DOX NPs. The method of synthesizing ZnO@polymer core−shell QDs was modified on the basis of our previous route.[42] Briefly, 2.33 g of zinc methacrylate was dissolved in 100 mL of ethanol at 80 °C, and then the solution was cooled to room temperature. Then, 0.13 g of 2, 2′-azobis(isobutyronitrile) (AIBN) and 15 mL of poly(ethylene glycol) methyl ether methacrylate were added into the solution, and the mixture was heated to 72 °C for 15 min. Afterward, 100 mL of 0.14 M LiOH ethanol solution was added into the reaction solution, followed by addition of another 0.13 g of AIBN. After a reflux period of 1 h, the solution was cooled and dialyzed against deionized water for 3 days. The concentrations of all NP samples were measured by freeze-drying the solutions and weighting the solid products.

The ZnO-Gd NPs were obtained by mixing 10 mL of ZnO@polymer QDs aqueous solution (0.94 mg/mL) with 2.35 mL of $GdCl_3$ aqueous solution (10 mM). The solution was stirred for 12 h and dialyzed against sodium citrate aqueous solution (1 mM) for 4 h and finally against deionized water for 2 days. The ZnO-Gd-DOX NPs were prepared by mixing 20 mL of ZnO-Gd NPs aqueous solution (0.48 mg/mL) with 2 mL of DOX aqueous solution (3.0 mg/mL). The solution was stirred for 12 h and then dialyzed against deionized water for 2 days.

The PL spectra were measured by a Horiba JobinYvon fluoromax-4 spectrofluorometer equipped with an F-3018 quantum yield accessory including an integrating sphere. The UV−vis absorption data were recorded by a Unico 2802 UV−vis spectrometer. Transmission electron microscope (TEM) images were obtained using a JEM-2010 transmission electron microscope operating at 200 kV. Dynamic light scattering (DLS) spectra and zeta potentials were measured on a Malvern ZS-90 Zetasizer. The relaxation times at low field strength of 0.55 T were measured on a MicroMRI instrument (Shanghai Niumag Corp.). T_1 measurements were performed by using an inversion recovery sequence with various inversion times, T_2 variation was determined by using the Carr−Purcell−Meiboom−Gill pulse sequence, and T_1-weighted MRI of the samples was obtained by the spin echo sequence.

The contrast abilities of the samples were evaluated by measuring the longitudinal relaxation rate $(1/T_1)$ and the transverse relaxation rate $(1/T_2)$ with various Gd^{3+} ion concentrations with a 0.55 T MRI system. The relaxivity (r_i, i = 1, 2) of the contrast agents were calculated according to the eq $(1/T_i)_{obs} = (1/T_i)_{dis} + r_i$ [M] (i = 1, 2), where $(1/T_i)_{obs}$ and $(1/T_i)_{dis}$ represent the observed solvent relaxation rate and the intrinsic diamagnetic solvent relaxation rate, respectively, and [M] is the Gd^{3+} ion concentration. It is known that the r value is proportional to the tumbling time τ_R, which can be enhanced by increasing the molecular size of the contrast agent. According to the Debye-Stokes equation $\tau_R = 4\pi\eta R^3/3k_BT$, where the dynamic viscosity η is 10^{-3} Pa·s, k_B is 4×10^{-21} J, R is the hydrodynamic radius of NPs, and T is 298 K, the tumbling time τ_R of ZnO-Gd-DOX NPs is calculated to be 1.5×10^{-9} s, which is ideal for obtaining suitable relaxivity at clinical magnetic field strengths. In addition, loading DOX renders R to increase for the NPs (Figure S2), while τ_R is proportional to R^3, and thus, r values of ZnO-Gd-DOX are larger than those of ZnO-Gd. The ratio of r_2/r_1 is a main parameter for MRI contrast agents, which means that the agents are suitable for T_1 or T_2 enhancement. For both ZnO-Gd and ZnO-Gd-DOX NPs, the r_2/r_1 values are 1.27 and 1.26, respectively, indicating they are T_1 (positive) MRI contrast agents. It should be mentioned that R values for those complexes are usually in the picosecond regime, *e.g.* 7×10^{-11} s for the clinical Gd-DTPA.

DOX Release. To study the DOX release in acetate buffer solution, 30 mg of ZnO-Gd-DOX NPs was dissolved in 3 mL of three kinds of buffer solutions (pH 5.0, 6.0, and 7.0), respectively. Then, it was sealed in a dialysis bag (molecular weight cutoff = 8000) and dialyzed against 20 mL of the corresponding buffer solution. During dialysis for 2 days, the outside buffer solution was exchanged by 20 mL of new buffer solution at different time intervals. The released DOX in the buffer solution was collected and its concentration was analyzed by UV−vis spectroscopy according to the typical DOX absorption at 480 nm. The amount of released DOX at different time intervals was normalized to the total amount accumulated in the buffer solutions.

MTT Assay of Cell Viability and Cell Imaging. All cell culture processes in this research were carried out with 5% CO_2 at 37 °C. BxPC-3 cells were seeded at 5×10^3 cells per well into a 96-well cell culture plate in DMEM (Dulbecco's modified Eagle medium) with 10% FBS (fetal bovine serum) for 24 h. Then, the culture medium was changed to be the culture medium containing DOX or NPs with various concentrations for another 24 h. Afterward, cells were incubated with 100 μL of new culture medium and 20 μL of MTT (thiazolyl blue tetrazolium bromide, 5 mg/mL in PBS) for 4 h. After the medium was removed, formazan crystals were dissolved with dimethyl sulfoxide (DMSO) for 10 min, and the absorbance of MTT at 492 nm was measured by an automatic scanning multiwall spectrometer (SPR-960, Sunostik).

BxPC-3 cells were seeded in glass dishes containing DMEM with 10% FBS for 24 h, and then cultured with ZnO-Gd-DOX NPs at a DOX concentration of 1 μg/mL for 1.5 h. After a wash with PBS (phosphate buffered saline) twice, the sample was embedded in DMEM solution for taking fluorescence images by a Leica TCS SP8 STED microscope with a 63×IMM objective (oil immersion) lens. The samples were excited by a laser of 488 nm and the emission spectra were collected within 570−620 nm.

Animal Experiments. BxPC-3 tumor-bearing nude mice were purchased from Shanghai SLAC Laboratory Animal Co., Ltd. Animal care and handing procedures were in agreement with the guidelines evaluated and approved by the ethics committee of Fudan University. The *in vivo* therapeutic efficacy of ZnO-Gd-DOX NPs was also investigated with BxPC-3 tumor-bearing nude mice. After the tumor sizes reached approximately 50 mm^3, the mice were divided into the following five groups for intratumor injections with different agents every 2 days: (1) saline; (2) ZnO-Gd-DOX NPs, each dosage of DOX is 2 mg/kg; (3) commercial DOXIL, each dosage of DOX is 2 mg/kg; (4) 2 mg/kg of free DOX; (5) ZnO-Gd NPs, each dosage of Zn^{2+} ions is 1.25 mg/kg, the same Zn^{2+} concentration as that in (2) ZnO-Gd-DOX NPs. Tumor sizes and body weights were monitored every 3 days within 36 days. The length and width of the tumors were measured by a digital caliper. The tumor volume was calculated according to the following formula: $\text{width}^2 \times \text{length}/2$.

A BxPC-3 tumor-bearing nude mouse was anesthetized using 100 μL of 5% chloral hydrate. MRI was conducted on a Siemens TrioTim 3T MRI scanner, using a 3D-FLASH. The mice were scanned before and after the injection of contrast agent. Then, 200 μL of ZnO-Gd-DOX NPs saline solution was injected into the tumor, and the dose was calculated to be 0.02 mmol Gd kg^{-1}. Fluorescence imaging was carried out on a Bruker *in vivo* FX PRO imaging system.

ICP-AES and Histology Analyses. To investigate the agent distribution in the organs, mice were sacrificed for careful necropsy after 36 days of treatment. The heart, liver, spleen, lung, tumor and kidneys were resected, rinsed with sterile physiological saline, and then blotted dry with filter paper. Afterward, the samples were freeze-dried at −80 °C for 24 h and then digested by *aqua regia* (5 mL for each

DOI: 10.1021/acsnano.5b07846
ACS Nano 2016, 10, 4294−4300

organ) at room temperature for 48 h. Zn and Gd content in the organs was determined by ICP-AES. For histopathological tests, the tissue samples were embedded in paraffin blocks, sectioned into 5 μm slices, and mounted onto the glass slides. After H&E staining, the sections were examined by an Olympus BX51 microscope.

HPLC Analyses. DOX concentration in livers was determined by High Performance Liquid Chromatography (HPLC). In brief, livers were homogenized with 2 mL of methanol using a high-speed tissue homogenizer in ice bath. Then, 50 μL of methanol and 50 μL (10 μg/mL) of daunorubicin (internal standard) were added in 1 mL of tissue homogenate. Three milliliters of the chloroform/methanol (volume ratio 4:1) mixture was used for extraction. After that the mixture was centrifuged for 10 min. The lower layer of organic phase was drained quantitatively and dried at 26 °C under nitrogen. The residue was dissolved in 60 μL of methanol. Finally, 50 μL of the sample was injected into HPLC system. The standard and control samples of the tissues for the drug analyses were prepared in the same manner. The mobile phase in HPLC consisted of acetonitrile and methanol, and the flow rate was kept at 1 mL/min. The effluent was excited at 480 nm.

ASSOCIATED CONTENT

Supporting Information

The Supporting Information is available free of charge on the ACS Publications website at DOI: 10.1021/acsnano.5b07846.

Additional experimental data (PDF)

AUTHOR INFORMATION

Corresponding Authors

*E-mail: jlkong@fudan.edu.cn.

*E-mail: hmxiong@fudan.edu.cn.

Notes

The authors declare no competing financial interest.

ACKNOWLEDGMENTS

This work was supported by National Major Basic Research Program of China (2013CB934101), the National Natural Science Foundation of China (21271045, 21335002, 21427806, 11074053 and 31170802), NCET-11-0115 and the Shanghai Leading Academic Discipline Project (B109).

REFERENCES

(1) Umar, A.; Dunn, B. K.; Greenwald, P. Future Directions in Cancer Prevention. *Nat. Rev. Cancer* **2012**, *12*, 835−848.

(2) Thompson, I. M.; Cabang, A. B.; Wargovich, M. J. Future Directions in the Prevention of Prostate Cancer. *Nat. Rev. Clin. Oncol.* **2014**, *11*, 49−60.

(3) Cleeland, C. S.; Allen, J. D.; Roberts, S. A.; Brell, J. M.; Giralt, S. A.; Khakoo, A. Y.; Kirch, R. A.; Kwitkowski, V. E.; Liao, Z. X.; Skillings, J. Reducing the Toxicity of Cancer Therapy: Recognizing Needs, Taking Action. *Nat. Rev. Clin. Oncol.* **2012**, *9*, 471−478.

(4) Liu, Q. L.; Jin, C.; Wang, Y. Y.; Fang, X. H.; Zhang, X. B.; Chen, Z.; Tan, W. H. Aptamer-Conjugated Nanomaterials for Specific Cancer Cell Recognition and Targeted Cancer Therapy. *NPG Asia Mater.* **2014**, *6*, e95.

(5) Ling, D.; Park, W.; Park, S. J.; Lu, Y.; Kim, K. S.; Hackett, M. J.; Kim, B. H.; Yim, H.; Jeon, Y. S.; Na, K.; Hyeon, T. Multifunctional Tumor pH-Sensitive Self-Assembled Nanoparticles for Bimodal Imaging and Treatment of Resistant Heterogeneous Tumors. *J. Am. Chem. Soc.* **2014**, *136*, 5647−5655.

(6) Abdukayum, A.; Yang, C.; Zhao, Q.; Chen, J.; Dong, L.; Yan, X. Gadolinium Complexes Functionalized Persistent Luminescent Nanoparticles as a Multimodal Probe for Near-Infrared Luminescence and Magnetic Resonance Imaging *in Vivo*. *Anal. Chem.* **2014**, *86*, 4096−4101.

(7) Zhao, Z. L.; Fan, H. H.; Zhou, G. F.; Bai, H. R.; Liang, H.; Wang, R. W.; Zhang, X. B.; Tan, W. H. Activatable Fluorescence/MRI Bimodal Platform for Tumor Cell Imaging *via* MnO_2 Nanosheet-Aptamer Nanoprobe. *J. Am. Chem. Soc.* **2014**, *136*, 11220−11223.

(8) Yao, J.; Yang, M.; Duan, Y. X. Chemistry, Biology, and Medicine of Fluorescent Nanomaterials and Related Systems: New Insights into Biosensing, Bioimaging, Genomics, Diagnostics, and Therapy. *Chem. Rev.* **2014**, *114*, 6130−6178.

(9) Wang, Y.; Huang, R. Q.; Liang, G. H.; Zhang, Z. Y.; Zhang, P.; Yu, S. N.; Kong, J. L. MRI-Visualized, Dual-Targeting, Combined Tumor Therapy Using Magnetic Graphene-Based Mesoporous Silica. *Small* **2014**, *10*, 109−116.

(10) Kang, B.; Li, J.; Chang, S. Q.; Dai, M. Z.; Ren, C.; Dai, Y. D.; Chen, D. Subcellular Tracking of Drug Release from Carbon Nanotube Vehicles in Living Cells. *Small* **2012**, *8*, 777−782.

(11) Xiao, Q.; Zheng, X.; Bu, W.; Ge, W.; Zhang, S.; Chen, F.; Xing, H.; Ren, Q.; Fan, W.; Zhao, K.; Hua, Y.; Shi, A. J. Core/Satellite Multifunctional Nanotheranostic for *in Vivo* Imaging and Tumor Eradication by Radiation/Photothermal Synergistic Therapy. *J. Am. Chem. Soc.* **2013**, *135*, 13041−13048.

(12) Chen, J.; Guo, Z.; Wang, H. B.; Gong, M.; Kong, X. K.; Xia, P.; Chen, Q. W. Multifunctional Fe_3O_4@C@Ag Hybrid Nanoparticles as Dual Modal Imaging Probes and Near-Infrared Light-Responsive Drug Delivery Platform. *Biomaterials* **2013**, *34*, 571−581.

(13) Vivero-Escoto, J. L.; Huxford-Phillips, R. C.; Lin, W. B. Silica-Based Nanoprobes for Biomedical Imaging and Theranostic Applications. *Chem. Soc. Rev.* **2012**, *41*, 2673−2685.

(14) Sanson, C.; Diou, O.; Thevenot, J.; Ibarboure, E.; Soum, A.; Brulet, A.; Miraux, S.; Thiaudiere, E.; Tan, S.; Brisson, A.; Dupuis, V.; Sandre, O.; Lecommandoux, S. Doxorubicin Loaded Magnetic Polymersomes: Theranostic Nanocarriers for MR Imaging and Magneto-Chemotherapy. *ACS Nano* **2011**, *5*, 1122−1140.

(15) Chen, H. Y.; Sulejmanovic, D.; Moore, T.; Colvin, D. C.; Qi, B.; Mefford, O. T.; Gore, J. C.; Alexis, F.; Hwu, S. J.; Anker, J. N. Iron-Loaded Magnetic Nanocapsules for pH-Triggered Drug Release and MRI Imaging. *Chem. Mater.* **2014**, *26*, 2105−2112.

(16) Zhang, Z. Y.; Xu, Y. D.; Ma, Y. Y.; Qiu, L. L.; Wang, Y.; Kong, J. L.; Xiong, H. M. Biodegradable ZnO@polymer CoreShell Nanocarriers: pH-Triggered Release of Doxorubicin *in Vitro*. *Angew. Chem., Int. Ed.* **2013**, *52*, 4127−4131.

(17) Sun, T.; Zhang, Y. S.; Pang, B.; Hyun, D. C.; Yang, M.; Xia, Y. Engineered Nanoparticles for Drug Delivery in Cancer Therapy. *Angew. Chem., Int. Ed.* **2014**, *53*, 12320−12364.

(18) Sun, H. Z.; Zhang, F.; Wei, H. T.; Yang, B. The Effects of Composition and Surface Chemistry on the Toxicity of Quantum Dots. *J. Mater. Chem. B* **2013**, *1*, 6485−6494.

(19) Wang, C.; Xu, H.; Liang, C.; Liu, Y. M.; Li, Z. W.; Yang, G. B.; Cheng, H.; Li, Y. G.; Liu, Z. Iron Oxide@Polypyrrole Nanoparticles as a Multifunctional Drug Carrier for Remotely Controlled Cancer Therapy with Synergistic Antitumor Effect. *ACS Nano* **2013**, *7*, 6782−6795.

(20) Tian, Y.; Jiang, X. J.; Chen, X.; Shao, Z. Z.; Yang, W. L. Doxorubicin-Loaded Magnetic Silk Fibroin Nanoparticles for Targeted Therapy of Multidrug-Resistant Cancer. *Adv. Mater.* **2014**, *26*, 7393−7398.

(21) Liu, Q.; Chen, M.; Sun, Y.; Chen, G. Y.; Yang, T. S.; Gao, Y.; Zhang, X. Z.; Li, F. Y. Multifunctional Rare-Earth Self-Assembled Nanosystem for Tri-modal Upconversion Luminescence/Fluorescence/Positron Emission Tomography Imaging. *Biomaterials* **2011**, *32*, 8243−8253.

(22) Wang, C.; Cheng, L.; Liu, Z. Upconversion Nanoparticles for Photodynamic Therapy and Other Cancer Therapeutics. *Theranostics* **2013**, *3*, 317−330.

(23) Tang, J.; Kong, B.; Wu, H.; Xu, M.; Wang, Y. C.; Wang, Y. L.; Zhao, D. Y.; Zheng, G. F. Carbon Nanodots Featuring Efficient FRET for Real-Time Monitoring of Drug Delivery and Two-Photon Imaging. *Adv. Mater.* **2013**, *25*, 6569−6574.

(24) Li, W.; Zhang, Z. H.; Kong, B. A.; Feng, S. S.; Wang, J. X.; Wang, L. Z.; Yang, J. P.; Zhang, F.; Wu, P. Y.; Zhao, D. Y. Simple and Green Synthesis of Nitrogen-Doped Photoluminescent Carbonaceous

DOI: 10.1021/acsnano.5b07846
ACS Nano 2016, 10, 4294−4300

Nanospheres for Bioimaging. *Angew. Chem., Int. Ed.* **2013**, *52*, 8151−8155.
(25) Wang, X. J.; Wang, C.; Cheng, L.; Lee, S. T.; Liu, Z. Noble Metal Coated Single-Walled Carbon Nanotubes for Applications in Surface Enhanced Raman Scattering Imaging and Photothermal Therapy. *J. Am. Chem. Soc.* **2012**, *134*, 7414−7422.
(26) Liu, Z.; Fan, A. C.; Rakhra, K.; Sherlock, S.; Goodwin, A.; Chen, X. Y.; Yang, Q. W.; Felsher, D. W.; Dai, H. J. Supramolecular Stacking of Doxorubicin on Carbon Nanotubes for *in Vivo* Cancer Therapy. *Angew. Chem., Int. Ed.* **2009**, *48*, 7668−7672.
(27) Yang, K.; Feng, L. Z.; Shi, X. Z.; Liu, Z. Nano-Graphene in Biomedicine: Theranostic Applications. *Chem. Soc. Rev.* **2013**, *42*, 530−547.
(28) Liu, Z.; Robinson, J. T.; Sun, X. M.; Dai, H. J. PEGylated Nanographene Oxide for Delivery of Water-Insoluble Cancer Drugs. *J. Am. Chem. Soc.* **2008**, *130*, 10876−10877.
(29) Li, X.; Zhou, L.; Wei, Y.; El-Toni, A. M.; Zhang, F.; Zhao, D. Anisotropic Growth-Induced Synthesis of Dual-Compartment Janus Mesoporous Silica Nanoparticles for Bimodal Triggered Drugs Delivery. *J. Am. Chem. Soc.* **2014**, *136*, 15086−15092.
(30) Kim, J.; Kim, H. S.; Lee, N.; Kim, T.; Kim, H.; Yu, T.; Song, I. C.; Moon, W. K.; Hyeon, T. Multifunctional Uniform Nanoparticles Composed of a Magnetite Nanocrystal Core and a Mesoporous Silica Shell for Magnetic Resonance and Fluorescence Imaging and for Drug Delivery. *Angew. Chem., Int. Ed.* **2008**, *47*, 8438−8441.
(31) Wang, Y.; Wang, K. Y.; Zhao, J. F.; Liu, X. G.; Bu, J.; Yan, X. Y.; Huang, R. Q. Multifunctional Mesoporous Silica-Coated Graphene Nanosheet Used for Chemo-Photothermal Synergistic Targeted Therapy of Glioma. *J. Am. Chem. Soc.* **2013**, *135*, 4799−4804.
(32) Topete, A.; Alatorre-Meda, M.; Iglesias, P.; Villar-Alvarez, E. M.; Barbosa, S.; Costoya, J. A.; Taboada, P.; Mosquera, V. Fluorescent Drug-Loaded, Polymeric-Based, Branched Gold Nanoshells for Localized Multimodal Therapy and Imaging of Tumoral Cells. *ACS Nano* **2014**, *8*, 2725−2738.
(33) Feng, L. Z.; Yang, X. Z.; Shi, X. Z.; Tan, X. F.; Peng, R.; Wang, J.; Liu, Z. Polyethylene Glycol and Polyethylenimine Dual-Functionalized Nano-Graphene Oxide for Photothermally Enhanced Gene Delivery. *Small* **2013**, *9*, 1989−1997.
(34) Krug, H. F. Nanosafety Research - Are We on the Right Track? *Angew. Chem., Int. Ed.* **2014**, *53*, 12304−12319.
(35) Som, C.; Nowack, B.; Krug, H. F.; Wick, P. Toward the Development of Decision Supporting Tools That Can Be Used for Safe Production and Use of Nanomaterials. *Acc. Chem. Res.* **2013**, *46*, 863−872.
(36) Krug, H. F.; Wick, P. Nanotoxicology: An Interdisciplinary Challenge. *Angew. Chem., Int. Ed.* **2011**, *50*, 1260−1278.
(37) Xiong, H. M. ZnO Nanoparticles Applied to Bioimaging and Drug Delivery. *Adv. Mater.* **2013**, *25*, 5329−5335.
(38) Zhang, H. J.; Xiong, H. M.; Ren, Q. G.; Xia, Y. Y.; Kong, J. L. ZnO@silica Core-Shell Nanoparticles with Remarkable Luminescence and Stability in Cell Imaging. *J. Mater. Chem.* **2012**, *22*, 13159−13165.
(39) Xiong, H. M. Photoluminescent ZnO Nanoparticles Modified by Polymers. *J. Mater. Chem.* **2010**, *20*, 4251−4262.
(40) Ilves, M.; Palomaki, J.; Vippola, M.; Lehto, M.; Savolainen, K.; Savinko, T.; Alenius, H. Topically Applied ZnO Nanoparticles Suppress Allergen Induced Skin Inflammation but Induce Vigorous IgE Production in the Atopic Dermatitis Mouse Model. *Part. Fibre Toxicol.* **2014**, *11*, 1−12.
(41) Szikszai, Z.; Kertesz, Z.; Bodnar, E.; Borbiro, I.; Angyal, A.; Csedreki, L.; Furu, E.; Szoboszlai, Z.; Kiss, A. Z.; Hunyadi, J. Nuclear Microprobe Investigation of the Penetration of Ultrafine Zinc Oxide into Human Skin Affected by Atopic Dermatitis. *Nucl. Instrum. Methods Phys. Res., Sect. B* **2011**, *269*, 2278−2280.
(42) Xiong, H. M.; Xu, Y.; Ren, Q. G.; Xia, Y. Y. Stable Aqueous ZnO@polymer Core-Shell Nanoparticles with Tunable Photoluminescence and Their Application in Cell Imaging. *J. Am. Chem. Soc.* **2008**, *130*, 7522−7523.
(43) Yang, Y. J.; Zhao, T.; Cheng, T.; Shen, J. M.; Liu, X. Y.; Yu, B. F.; Lv, S. Y.; Zhang, H. X. Hepatotoxicity Induced by ZnO Quantum Dots in Mice. *RSC Adv.* **2014**, *4*, 5642−5648.
(44) Hong, T. K.; Tripathy, N.; Son, H. J.; Ha, K. T.; Jeong, H. S.; Hahn, Y. B. A Comprehensive *in Vitro* and *in Vivo* Study of ZnO Nanoparticles Toxicity. *J. Mater. Chem. B* **2013**, *1*, 2985−2992.
(45) Yang, Y. J.; Lan, J. F.; Xu, Z. G.; Chen, T.; Zhao, T.; Cheng, T.; Shen, J. M.; Lv, S. Y.; Zhang, H. X. Toxicity and Biodistribution of Aqueous Synthesized ZnS and ZnO Quantum Dots in Mice. *Nanotoxicology* **2014**, *8*, 107−116.
(46) Cho, N. H.; Cheong, T. C.; Min, J. H.; Wu, J. H.; Lee, S. J.; Kim, D.; Yang, J. S.; Kim, S.; Kim, Y. K.; Seong, S. Y. A Multifunctional Core-Shell Nanoparticle for Dendritic Cell-based Cancer Immunotherapy. *Nat. Nanotechnol.* **2011**, *6*, 675−682.
(47) Wang, Y. H.; Song, S. Y.; Liu, J. H.; Liu, D. P.; Zhang, H. J. ZnO-Functionalized Upconverting Nanotheranostic Agent: Multi-Modality Imaging Guided Chemotherapy with On-Demand Drug Release Triggered by pH. *Angew. Chem., Int. Ed.* **2015**, *54*, 536−540.
(48) Muhammad, F.; Guo, M. Y.; Guo, Y. J.; Qi, W. X.; Qu, F. Y.; Sun, F. X.; Zhao, H. J.; Zhu, G. S. Acid Degradable ZnO Quantum Dots as a Platform for Targeted Delivery of an Anticancer Drug. *J. Mater. Chem.* **2011**, *21*, 13406−13412.
(49) Liu, Y. L.; Ai, K. L.; Yuan, Q. H.; Lu, L. H. Fluorescence-Enhanced Gadolinium-Doped Zinc Oxide Quantum Dots for Magnetic Resonance and Fluorescence Imaging. *Biomaterials* **2011**, *32*, 1185−1192.
(50) Werner, E. J.; Datta, A.; Jocher, C. J.; Raymond, K. N. High Relaxivity MRI Contrast Agents: where Co-ordination Chemistry Meets Medical Imaging. *Angew. Chem., Int. Ed.* **2008**, *47*, 8568−8580.
(51) Caravan, P. Protein-Targeted Gadolinium-Based Magnetic Resonance Imaging (MRI) Contrast Agents: Design and Mechanism of Action. *Acc. Chem. Res.* **2009**, *42*, 851−862.
(52) Caravan, P. Strategies for Increasing the Sensitivity of Gadolinium Based MRI Contrast Agents. *Chem. Soc. Rev.* **2006**, *35*, 512−523.
(53) Liang, G. H.; Ye, D. X.; Zhang, X. X.; Dong, F.; Chen, H.; Zhang, S.; Li, J. Q.; Shen, X. R.; Kong, J. L. One-Pot Synthesis of Gd^{3+}-Functionalized Gold Nanoclusters for Dual Model (Fluorescence/Magnetic Resonance) Imaging. *J. Mater. Chem. B* **2013**, *1*, 3545−3552.

DOI: 10.1021/acsnano.5b07846
ACS Nano 2016, 10, 4294−4300